Anomalous magnetism in the $3d$-$4f$ double perovskite oxide Nd_2FeCrO_6 with the Kramers ion Nd^{3+}

Saurav Kumar,[1] Shantanu Majumder,[1] Francesco Congiu,[2] Giuseppe Muscas,[2] H. Luetkens,[3] S. D. Kaushik,[4] Shishir K. Pandey,[5] Stephen L. Lee,[6] Uday Deshpande,[7] Tapati Sarkar,[8,*] and Soumya Jyoti Ray[1,†]

[1]*Department of Physics, Indian Institute of Technology Patna, Bihta 801106, India*

[2]*Department of Physics, University of Cagliari, Cittadella Universitaria di Monserrato, S. P. 8 Km 0.700, I-09042 Monserrato, CA, Italy*

[3]*Laboratory for Muon Spin Spectroscopy, Paul Scherrer Institute, CH-5232, Villigen PSI, Switzerland*

[4]*UGC-DAE Consortium for Scientific Research Mumbai Centre, BARC Campus, Trombay, Mumbai 400085, India*

[5]*Department of General Sciences (Physics), Birla Institute of Technology and Science, Pilani, Dubai Campus, Dubai International Academic City, Dubai 345055 United Arab Emirates*

[6]*School of Physics and Astronomy, SUPA, University of St. Andrews, St. Andrews KY16 9SS, United Kingdom*

[7]*UGC-DAE Consortium for Scientific Research, Indore Centre, University Campus, Khandwa road, Indore 452001, India*

[8]*Department of Materials Science and Engineering, Box 35, Uppsala University, SE-751 03 Uppsala, Sweden*

(Received 21 March 2025; revised 15 June 2025; accepted 17 June 2025; published 12 August 2025; corrected 23 January 2026)

The complex magnetic behavior of double-perovskite oxides ($A_2BB'O_6$) with rare-earth (RE) element A and transition metal (TM) elements B-B′ is determined by the interactions between intra- and interatomic magnetic moments. The peculiar magnetism in these systems stems from the interplay between spin, orbit, and lattice degrees of freedom. This study comprehensively investigates the role of spin-orbit entangled $J_{\text{eff}} = 1/2$ moments of the Kramers ion Nd^{3+} on the magnetic ground state of a B-site ordered ferrimagnetic (FiM) double-perovskite oxide, Nd_2FeCrO_6. Furthermore, employing microscopic techniques like μSR (muon spin rotation and relaxation) and neutron diffraction, we gained insight into the origin of low-temperature anomalies in the magnetic ground state of the system. The DC magnetization data encompass the first transition at critical temperature $T_N = 250$ K, followed by a negative magnetization below 15 K. The temperature-dependent neutron diffraction shows a commensurate magnetic ordering below 250 K, forming a ferrimagnetic ground state, supported by theoretical calculations. In addition, a sharp drop in initial muon asymmetry confirms the transition from a disordered state to a long-range-ordered state at 250 K. Interestingly, the thermal evolution of the dynamic muon spin-relaxation rate (λ_L) reveals a transition at two temperatures, at 250 K and ≈ 11 K, suggesting a low-T ordering at the A site. The heat-capacity data show that Nd^{3+} hosts the ground-state doublet (pseudospin-1/2) at low temperatures. Our analysis of neutron diffraction, heat capacity, and μSR results suggests that the correlation between the Nd^{3+} doublet and the complex interaction between Nd-TM moments gives rise to the observed low-temperature anomaly.

DOI: 10.1103/c87f-xf83

I. INTRODUCTION

The interplay of charge, spin, and orbital degrees of freedom in transition metal (TM) compounds gives rise to many exotic phenomena such as spin-orbit driven magnetic states [1], spin-liquid like states induced by mixing d^{10}–d^0 cations [2], etc. These systems stand out as a test ground for understanding fundamental physics and for realizing next-generation devices, for example, spintronics devices [3,4]. In this context, TM-based double-perovskite oxides (DP) with composition $A_2BB'O_6$, where A is a rare-earth (RE) element and B and B′ are TM elements, have been extensively studied due to their multifunctional properties. Of particular significance, these compounds have been found or predicted to host an array of exotic states of matter, including superconductivity [5], half-metallicity [6], magnetoresistance [7], spin liquid [8] and spin-glass [9] behavior. Notably, their behavior can be manipulated by various stimuli such as strain, electric fields, and magnetic fields and intrinsic factors such as spin-orbit coupling, crystal fields, the Jahn-Teller effect, spin correlations, and frustration [10–14]. The intricate interplay of these factors allows tuning of both electrical and magnetic properties within the system.

In rare-earth elements, $4f$ electrons are more localized and have stronger spin-orbit coupling (SOC) than $4d$ or $5d$ elements. Under the effect of the crystal electric field (CEF), the $(2J + 1)$-fold spin degeneracy of spin-orbit coupled total angular momentum J is lifted and the energy levels of RE ions like Nd^{3+}, Sm^{3+}, etc. are split into doubly degenerate states, also known as a Kramers doublet. The ground-state doublet can be treated as pseudospin-1/2 [15]. In this context, DPs with rare-earth metals [16] deserve special attention, as the interaction between pseudospin-1/2 local moments can

*Contact author: tapati.sarkar@angstrom.uu.se

†Contact author: ray@iitp.ac.in; ray.sjr@gmail.com

influence the low-temperature properties and induce various exotic states in the system [17]. Moreover, intriguing physics may arise when strongly correlated $3d$ ions with no orbital moment coexist with $4f$ ions having strong SOC. Although several Kramers' ion-based DP have been synthesized and studied for their multifunctional properties [18], systems with neodymium (Nd) at the A site deserve special attention due to anomalous magnetic behavior such as negative magnetization, coupled spin ordering between Nd and TM atoms, and multiple magnetic ordering observed in various Nd-based DP systems (in combination with magnetic and nonmagnetic atoms at the B and/or B′ site) [19,20]. However, opinions on the fundamental origin of the second transition or downturn observed in these systems are not unanimous. For example, in Nd_2NiMnO_6, some reports suggest that the second transition related to the ferromagnetic ordering of the Nd moments is responsible for the downturn in magnetization [21]; on the other hand, Pal *et al.* explained this as the induced ordering of Nd moments in the internal field of Ni-Mn sublattice [22]. In some other systems like Nd_2NiIrO_6 [23], a second AFM ordering is reported. Since the magnetic behavior of rare-earth ions is very sensitive to the other magnetic ions present in the system, the nature of such anomalies is worth investigating from a fundamental physics perspective. This motivated us to investigate another Nd-based double-perovskite oxide that contains TM atoms at the B and B′ sites.

Here, we report a comprehensive study of Nd_2FeCrO_6 (NFCO). As a member of the RE_2FeCrO_6 [24] family, NFCO is anticipated to exhibit unique ferrimagnetic semiconductor properties, including a net magnetic moment of approximately $\approx 2\ \mu_B$ and an electronic band gap of ≈ 1.8 eV. These characteristics make NFCO a promising candidate for applications in spintronics, magnetic sensors, and energy-efficient electronic devices. By employing a comprehensive suite of advanced macroscopic and microscopic experimental techniques, this study aims to unravel the fundamental physical properties of NFCO, thereby contributing to a broader understanding of double-perovskite oxides and paving the way for future innovations in material science and technology.

II. EXPERIMENTAL AND THEORETICAL DETAILS

A single-phase high-quality polycrystalline sample of Nd_2FeCrO_6 (NFCO) was prepared using the solid-state reaction method by mixing the stoichiometric amount of Nd_2O_3, Cr_2O_3, and Fe_2O_3 powder. The mixture was calcined in the air between 1100 and 1300 °C with several intermediate grindings. Structural characterization was performed using x-ray diffraction [PANalytical x-ray diffractometer with Cu K_α (λ = 1.54 Å) radiation (45k V, 40 mA)] and neutron diffraction by employing PD 3 neutron powder diffractometer, installed by UGC-DAE CSR Mumbai Centre at Dhruva Reactor, Trombay, India. Magnetic measurements were carried out using the Physical Property Measurement System (PPMS DynaCool from Quantum Design, Inc.) in the temperature range of 5 to 390 K. The zero-field heat capacity was measured by the relaxation method in the temperature range of 5 to 300 K using the heat capacity option in the PPMS. The elemental composition and chemical states of the elements were investigated using the x-ray photoelectron spectrometer (SPECS, Germany, equipped with an Al K x-ray source (1486.61 eV) with a voltage of 13 kV and a power of 100 W) at the UGC-DAE Consortium for Scientific Research (CSR), Indore Centre, India. The optical band gap of the synthesized material was estimated from the ultraviolet-visible spectra using the Shimadzu UV-3101PC UV-visible spectrometer.

Powder neutron-diffraction measurements were performed to explore the evolution of the magnetic structure as a function of temperature (measured at powder diffractometer PD3 at the Dhruva reactor, Trombay, India) using a neutron beam of constant wavelength (λ = 1.48 Å). Approximately 4 g of sample was filled in a vanadium can, cooled in a closed refrigerator-based cryogen-free low-temperature system (M/s Cryogenic Ltd, UK). The diffraction experiments were carried out in a warming cycle, and the temperature was stabilized before data collection. The μSR experiments were carried out using the General Purpose Surface muon instrument (GPS spectrometer) at the Paul Scherrer Institute (PSI), Switzerland. The zero-field (ZF) and weak transverse field (wTF) measurements were performed in the temperature range of 5 to 480 K. A transverse field of 30 Oe was applied perpendicular to the initial polarization of the muon spin for the weak transverse field (wTF) measurements. X-ray and neutron-diffraction data were analyzed using the Rietveld refinement method using the FULLPROF package [25,26]. μSR data analysis was performed using MUSRFIT software [27].

Density functional theory (DFT) calculations were performed using the projector-augmented wave (PAW) method [28,29], implemented within the Vienna *ab initio* simulation package (VASP) [30]. The Perdew-Burke-Ernzerhof functional [31] was used within the generalized gradient approximation (GGA) of the exchange correlation functional. We started with the experimental lattice parameters of the monoclinic crystal structure with space group $P2_1/n$ (No. 14) which are $|\mathbf{a}|$ = 5.438 Å, $|\mathbf{b}|$ = 5.534 Å, and $|\mathbf{c}|$ = 7.729 Å. In our calculation, the plane-wave cutoff energy of 800 eV and $5 \times 5 \times 3$ Monkhorst-Pack scheme for k-mesh sampling of the Brillouin zone are considered. To account for the electronic correlation at the Fe and Cr sites, we employ the Dudarev scheme [32] of the DFT + U approach in our calculations with on-site Coulomb interactions $U_{\mathrm{Fe}} = 3.75$ eV and $U_{\mathrm{Cr}} = 2.75$ eV. The values of U are chosen to reproduce the experimentally observed band gap of 1.8 eV. We optimized the lattice parameters for the experimentally proposed magnetic ground state by imposing energy and force convergence criteria to be 10^{-5} eV and 10^{-2} eV/Å, respectively. The results are converged with respect to these parameters. Changes in the lattice constants are found to be <1.8%, with the maximum change occurring for b. Since the experimental and optimized lattice constants are quite close, we used the former for further calculations.

To estimate the first-neighbor Fe-Cr magnetic interaction $J_{\text{Fe-Cr}}$, which we later showed to be sufficient to describe the magnetic ordering in Nd_2FeCrO_6, the total energy of the experimentally observed magnetic ground state (E_{expt}) and ferromagnetic state (E_{ferro}) are calculated. The results were projected onto a Heisenberg model as

$$E_{\mathrm{expt}} = E_0 + \frac{6 \times J_{\text{Fe-Cr}}}{2} S_{\mathrm{Fe}} S_{\mathrm{Cr}},$$

$$E_{\mathrm{ferro}} = E_0 - \frac{6 \times J_{\text{Fe-Cr}}}{2} S_{\mathrm{Fe}} S_{\mathrm{Cr}}.$$

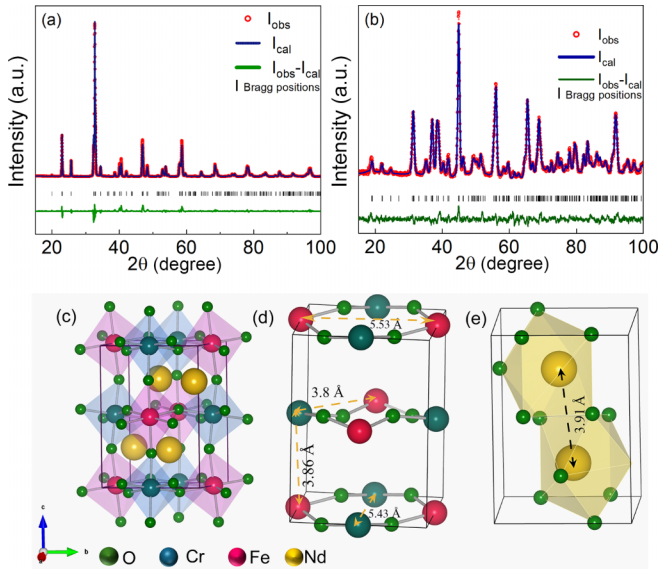

FIG. 1. (a) Rietveld refined room-temperature x-ray powder diffraction pattern of NFCO with $P2_1/n$ space group and (b) Rietveld refined (nuclear phase) neutron-diffraction pattern of NFCO at 290 K with $P2_1/n$ space group. Here, red open circles denote observed intensity I_{obs}, blue solid line represents calculated intensity I_{cal}, black vertical sticks are the allowed Bragg reflections, and the bottom green line is the difference between observed and calculated intensity $I_{obs} - I_{cal}$. (c) Crystal structure of Nd_2FeCrO_6 having chromium (cyan) and iron (pink sphere) atoms surrounded by oxygen (green sphere) atoms forming an octahedral environment. (d) Chromium and iron sublattices in the unit cell, the dashed yellow line represents the distance between the atoms in the unit cell. (e) Representative illustration of the position(s) of neodymium atoms in the unit cell.

Above, E_0 represent the nonmagnetic contributions to the total energy, and S_{Fe} and S_{Cr} are the spins on the Fe and Cr sites, respectively, and $J > 0$ for the ferromagnetic case. The use of the Heisenberg model above is justified as the largest change in the magnetic moments that occur for Cr is $\approx 8\%$ in the two magnetic configurations. We then absorb S_{Fe} and S_{Cr} into J and treat these as vectors of unit magnitude, i.e., $|S_{Fe}| = |S_{Cr}| = 1$. Using the above two equations, we obtain $J_{Fe\text{-}Cr}$, which is used further in the Monte Carlo (MC) simulation to determine T_N. In our in-house Monte Carlo (MC) code, unit vectors on a simple cubic lattice of $16 \times 16 \times 16$ are considered, and starting from a random spin configuration, the system is brought into thermal equilibrium within 2×10^5 MC steps at each temperature. After thermal equilibrium was achieved, we calculated the magnetization of each sublattice, which was further used to determine T_N. Our results have well-converged with respect to the lattice size and number of MC steps.

III. RESULTS

A. Structure and electronic properties

X-ray diffraction (XRD) and neutron-diffraction measurements were employed to investigate the structural properties of Nd_2FeCrO_6. The Rietveld refined room-temperature x-ray diffraction pattern is illustrated in Fig. 1(a). The absence of extra unfitted reflections indicates the single-phase purity of the sample. To determine the crystal structure, the XRD pattern profile was refined using monoclinic $P2_1/n$ (14) and orthorhombic *Pbnm* (62) space groups. The similarity between the monoclinic and orthorhombic space groups makes it difficult to distinguish between them using XRD, subject to incomplete ordering and β being very close to 90° [33]. Therefore, neutron-diffraction measurements were also carried out as a complementary tool to overcome this difficulty using a neutron beam of wavelength $\lambda = 1.48$ Å. Figure 1(b) displays the Rietveld refined neutron diffraction pattern measured at a temperature of 290 K. The appearance of the {011} peak at $2\theta = 18.76°$, which is forbidden in the *Pbnm* space group (shown in Fig. S1 in the Supplemental Material [34] for additional information regarding the claims made in the main paper), along with the {101} peak at $2\theta = 18.98°$ confirms the monoclinic structure of NFCO. The monoclinic angle β was found to be approximately $\approx 90.02°$ and the maximum bond angle between Fe-O-Cr $\approx 153.68°$. Figures 1(c)–1(e) represents the crystal structure and the position of atoms in the unit cell of the compound. The refinement parameter details (Table TI) and the thermal variation of the lattice parameters (Fig. S4) can be found in the Supplemental Material. While cell parameters **a** and **c** decrease with decreasing temperature, parameter **b** remains almost constant up to a temperature of 45 K; below this, it decreases slightly. X-ray photoelectron spectroscopy (XPS) measurements were performed at room temperature to probe the valency and ligand coordination of the participating elements of the compound. The results of the XPS analysis confirm the nominal valency, with 3+ charge state for Nd, Fe, and Cr, and 2^- for O. The details of the analysis are provided in the Supplemental Material [34].

B. Magnetic properties

To explore the magnetic ground-state of the system, we performed DC magnetization measurements as a function of temperature and applied magnetic field. Figure 2(a) shows the temperature dependence of the DC magnetization of NFCO in the temperature range of 5 to 390 K in the presence of an externally applied field of 100 Oe. For better understanding of the magnetic behavior of the system, magnetization (M) was measured under different conditions: (a) pre-ZFC (data collected while cooling the sample in the absence of an external field), (b) zero-field-cooled (ZFC), and (c) field-cooled conditions (both during the cooling (FCc) and in the subsequent warming process (FCw). Around 250 K temperature, a bifurcation is observed between the ZFC and FC magnetization curves, indicating the onset of a long-range magnetic order. Anticipating the results of the neutron-diffraction study (presented later), this feature corresponds to the Néel temperature of the ferrimagnetic ordering of Fe and Cr ions. Furthermore, reducing the temperature, in all curves, the value of M increases gradually, achieving a broad maximum at $T \approx 50$ K. Below this temperature, the pre-ZFC and FC curves exhibit a compensation point, a characteristic feature of ferrimagnetic structures. This indicates the presence of a low-temperature magnetization component that aligns antiparallel to the primary magnetic lattice. Additionally, the magnetization does not fall to zero at high temperatures. A small but

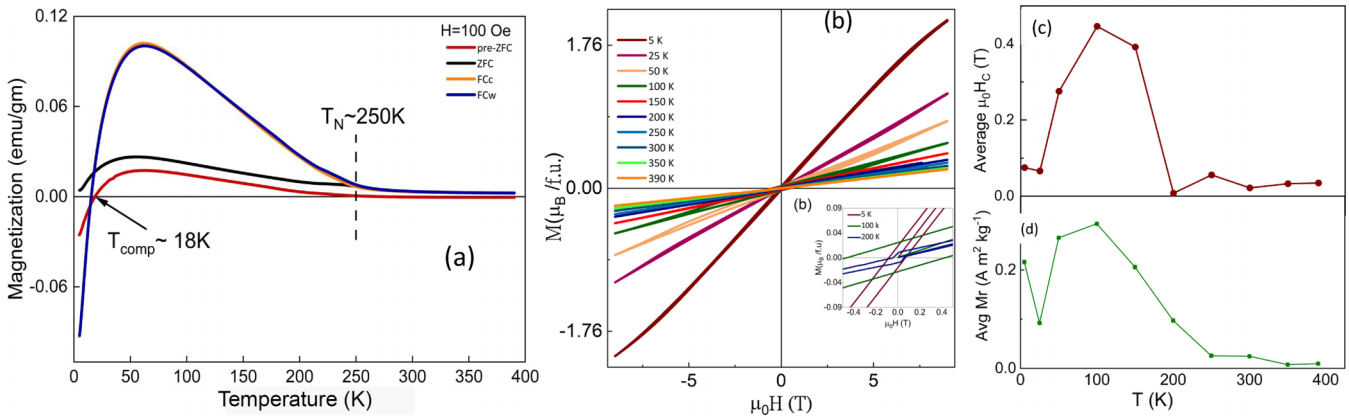

FIG. 2. (a) Temperature dependence of dc magnetization of NFCO measured under different conditions at an applied dc magnetic field of 100 Oe: prezero-field cooled (pre-ZFC) indicated by red, zero-field cooled (ZFC) indicated by black, field-cooled cooling (FCc) indicated by yellow and field-cooled warming (FCw) represented by blue. T_N represents Ferrimagnetic (FiM) Néel temperature and T_{comp} is the compensation temperature. (b) Field dependence of isothermal DC magnetization (M-H) of NFCO under zero-field-cooled conditions, measured at selected temperatures. The inset shows a magnified view of the M-H curve, near the origin, at 5, 100, and 200 K. (c) Temperature dependence of average coercive field (HC) and (d) average remanent magnetization.

significant magnetization tail persists well above the ordering temperature, hinting towards a residual ferromagnetic-like order in the system. Inverse susceptibility data (see Fig. S4) fitted in the high-temperature range (above 300 K) with the Curie-Weiss (CW) law yields CW temperature $\theta_{CW} \approx -24.6$ K and effective magnetic moment $\mu_{\text{eff}} = 0.7469\mu_B$. The value of the effective magnetic moment obtained is unexpectedly low, possibly due to the poor linearity of the curve at high temperatures. At higher applied fields of 500 Oe $\leqslant H \leqslant$ 1000 Oe, very rich magnetic features are observed in the ZFC data. At 100 Oe, after the first transition takes place at T_N, the magnetization measured under the ZFC condition increases continuously up to a temperature $\approx$ 50 K, followed by a gradual decrease with temperature. Interestingly, the magnetization takes an upturn below a temperature of 15 K, as shown in Fig. S5 in the Supplemental Material [34]. This indicates that the applied field is strong enough to rotate some anti-aligned moments in the field direction under such conditions. Here, it should be noted that the position of the compensation temperature T_{comp} gets shifted towards a lower temperature with increasing applied magnetic field. Similar behavior has also been observed in other DP systems [35,36].

To further understand the magnetic behavior, we performed isothermal magnetization measurements as a function of the applied magnetic field at selected temperatures, illustrated in Fig. 2(b). It exhibits an approximately linear response of magnetization with the applied magnetic field, similar to a paramagnet, up to a temperature of 250 K. As the temperature is further reduced, a deviation from linearity is observed and the hysteresis loop opens up, which remains unsaturated up to the highest applied magnetic field ($\pm$9 T). Also, a successive decrease in temperature exhibits an enhancement in the nonsaturation of the magnetization value. A closer look at the M-H loop shows that the remanent magnetization and coercivity increase with decreasing temperature down to 100 K. Surprisingly, a further decrease in temperature diminishes the hysteresis behavior, as shown in the inset of Fig. 2(b). In addition, reducing the temperature from 25 to 5 K shows a significant enhancement of the magnetization, which is reached at an applied field of 9 T. The thermal evolution of parameters extracted from the M-H curve, such as coercive field H_c and remanent magnetization M_r, presented in Figs. 2(c) and 2(d), also shows enhancement below 15 K.

C. Heat Capacity

To gain further insight into the ground-state behavior and magnetic ordering in detail, we measured the temperature dependence of the zero-field heat capacity $C_p(T)$ of Nd_2FeCrO_6 in a temperature range between 5 and 300 K. As depicted in Fig. S6, no lambda-like (λ-like) peak was detected at the transition temperature, which is expected for a long-range ordered system.

In addition to this, a broad peak appears between 270 and 300 K due to the uncompensated contribution of the grease used to make thermal contact [37]. The overall nature of the heat-capacity curve follows the Dulong-Petit law, and the heat capacity reaches the classical value of $3R$ per atomic site in the formula unit. To obtain detailed features of the curve at low temperatures, data were collected with a 1 K step between 5 and 75 K. As shown in Fig. 3(a), a hump-like feature below 15 K with a maximum at around a temperature of 8 K was observed. Furthermore, to estimate the contributions from the lattice phonon and magnetic components, we divided the $C_p(T)$ data into two regions: (a) temperature above 20 K and (b) between 5 and 20 K. The first region above 20 K is dominated by the lattice phonon contribution, which was modeled by equation (1) and contains one term of the Debye function and two terms of the Einstein function as given below:

$$C_{\text{lat}}(T) = C_D\left[9R\int_0^{\theta_D}\left(\frac{T}{\theta_D}\right)^3\frac{x^4e^x}{(e^x-1)^2}dx\right] + \sum_{i=1}^{2}C_{E_i}\left[3R\left(\frac{\theta_{E_i}}{T}\right)^2\frac{e^{\theta_{E_i}/T}}{\left(e^{\theta_{E_i}/T}-1\right)^2}\right], \quad (1)$$

where θ_D is the Debye temperature and $x = \frac{\hbar w}{k_B T}$. The red line in Fig. 3(a) indicates the fit obtained with coefficients C_D,

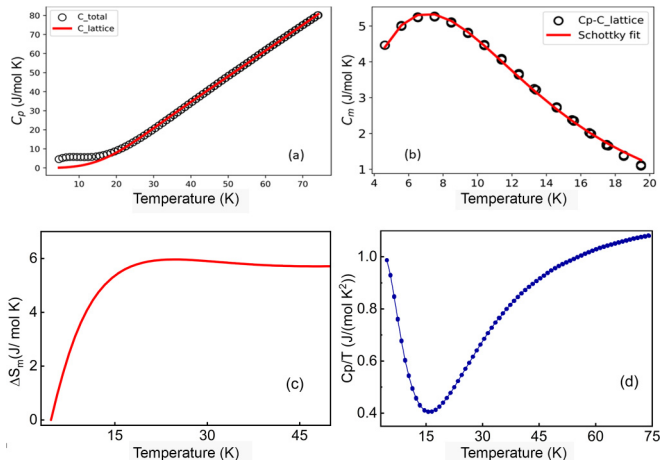

FIG. 3. (a) Temperature dependence of zero-field heat capacity C_p measured in the temperature range of 5 to 75 K. Black circles indicate total heat capacity measured, the solid red line represents the fit made with lattice contribution to the heat capacity, using combined Debye and Einstein model. (b) Temperature dependence of the magnetic contribution to the heat capacity. The red solid line represents the corresponding fit made using a two-level Schottky model. (c) Temperature dependence of change in magnetic entropy (ΔS_m) and (d) (C_p/T) as a function of temperature.

C_{E_1}, and C_{E_2} fixed in the ratio of 3 : 3 : 4. The values of the obtained parameters θ_D, θ_{E_1}, and θ_{E_2} are approximately 176, 336, and 449 K, respectively. Below 20 K, the fit deviates from the experimental data. The magnetic contribution to the heat capacity $C_m(T)$, depicted in Fig. 3(b), was obtained after subtracting the calculated lattice part ($C_{lattice}$) from C_p. The presence of a magnetic contribution to the heat capacity indicates some spin correlations in this range. The magnetic entropy provides insight into the ground-state properties. To quantify the change in magnetic entropy (ΔS_m), the integral of $C_m(T)/T$ over T was calculated. As shown in Fig. 3(c), the value of ΔS_m was found to be saturated at about 5.7 J/(mol K). In Kramers' ion with an odd number of $4f$ electrons such as Nd^{3+} ($4f^3$), splitting the spin-orbit-coupled moment J produces doublets, which in the ground states are considered pseudospin-1/2 moments ($J_{\text{eff}} = 1/2$) [17,38]. The obtained value of ΔS_m is equal to the expected value of $\approx R \ln 2$ for the $J_{\text{eff}} = 1/2$ state. This indicates the presence of a Kramer's doublet ground state of Nd^{3+} in Nd_2FeCrO_6. Moreover, Fig. 3(d) shows the dependance of (C_p/T) as a function of temperature where an upturn is observed below 14 K. This can be considered to arise from the magnetic correlation between $J_{\text{eff}} = 1/2$ moments, which reduces the entropy associated with the transition. Therefore, these features are probably signatures of the ordering of $J_{\text{eff}} = 1/2$ moments of the Nd^{3+} ion.

The broad hump in $C_p(T)$ may also be attributed to the Schottky anomaly observed for the Nd^{3+} ion [39] having origin in the Zeeman splitting of the ground-state doublet. In the absence of an external field, the internal field of the system may cause this splitting, thus lifting the ground-state degeneracy. A fit to the data with a two-level Schottky function, using Eq. (2), is shown by the solid red line in Fig. 3(b):

$$C_{\text{sch}} = \sum_{i=1}^{2} C_i \left[R \left(\frac{\Delta_{E_i}}{K_B T} \right)^2 \frac{e^{\Delta_{E_i}/K_B T}}{(e^{\Delta_{E_i}/K_B T} + 1)^2} \right]. \quad (2)$$

The obtained value of zero-field splitting was found to be $\Delta_{E_1}/k_B = 0.4$ K and $\Delta_{E_2}/k_B = 0.2$ K, respectively.

D. Neutron diffraction

To explore the origin of the anomaly observed in DC magnetization, heat capacity, and to identify the magnetic structure of the ground state, temperature-dependent powder neutron-diffraction (PND) measurements were performed between a temperature range of 3 and 290 K with $\lambda = 1.48$ Å. Figure 4(a) illustrates the evolution of the diffraction peak profile as a function of 2θ for data collected at different temperatures. Comparing the thermal dependencies of the diffraction peak profile reveals a gain in intensity in the {011} and {013} peaks with decreasing temperature. Additionally, at 3 K, two more reflections are visible at $2\theta = 15.5^\circ$ and 27°. These low-temperature peaks can be associated with rare-earth ion ordering.

A propagation vector $k = (0\,0\,0)$ was identified using the K-search option in FULLPROF. Magnetic symmetry analysis using the BasIreps program [40] within the FULLPROF package was used to find the allowed irreducible representation (IR) and the corresponding magnetic basis vectors (BVs). Considering the magnetic moment on the Fe, Cr, and Nd atoms, the

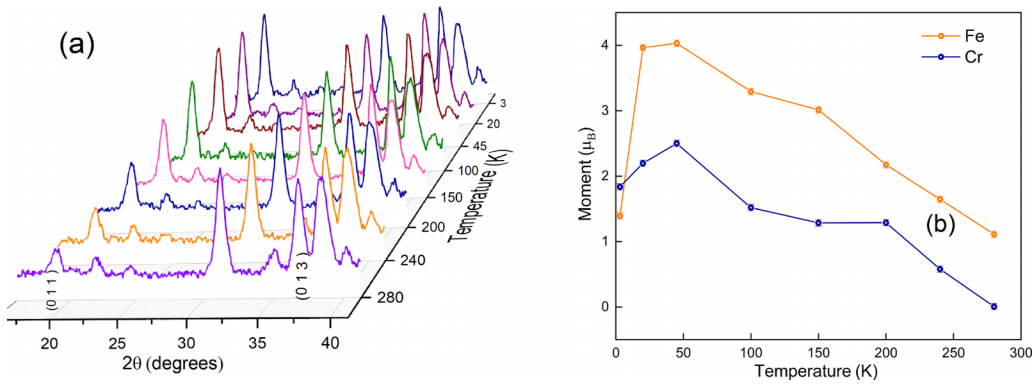

FIG. 4. (a) Evolution of NFCO neutron-diffraction pattern as a function of diffraction angle 2θ and temperature. (b) Thermal evaluation of magnetic moments of Fe (yellow curve) and Cr (blue curve) atoms obtained from the magnetic refinement of neutron-diffraction data.

TABLE I. Basis vectors for the allowed irreducible representations for propagation vector $k = (0\,0\,0)$ for 2b, 2d, and 4e sites.

Wyckoff position	Symmetry	IR1	IR3
		BV1 BV2 BV3	BV1 BV2 BV3
(Fe)2b, Cr(2d)	(x, y, z)	1 0 0 0 1 0 0 0 1	1 0 0 0 1 0 0 0 1
	$(-x+1/2, y+1/2, -z+1/2)$	−1 0 0 0 1 0 0 0 −1	1 0 0 0 −1 0 0 0 1
(Nd)4e	(x, y, z)	1 0 0 0 1 0 0 0 1	
	$(-x+1/2, y+1/2, -z+1/2)$	−1 0 0 0 1 0 0 0 −1	
	$(-x+1, -y+1, -z+1)$	1 0 0 0 1 0 0 0 1	
	$(x+1/2, -y+1/2, -z+1/2)$	−1 0 0 0 1 0 0 0 −1	

representation analysis for the propagation vector $k = (0\,0\,0)$ gives two identical IR, IR1, and IR3, for magnetic site 2b (0.5 0 0) and 2*d* (0.5 0 0.5), and four IR for Nd at general site 4e (Table I, for the 4e site only IR1 is listed). While IR1 contains FM coupling along the **b** axis and AFM coupling along the **a** and **c** axes, IR3 is FM in nature along the **a** and **c** axes and AFM along the **b** axis. The basis vectors of IR1 and IR3 for both sites differ in the orientation of moments only; however, the magnetic peak position suggests that IR1 is a suitable solution. The temperature dependence of the total magnetic moments on the Fe and Cr sites, determined from the magnetic refinement of the data, is shown in Fig. 4(b). At 45 K, the estimated magnetic moment values of the Fe and Cr atoms reach $\approx 4.0\mu_B$ and $2.5\mu_B$, respectively, which are close to the theoretically predicted values [41]. Surprisingly, at base temperature, the moment on the Fe and Cr atoms decreases to $\approx 1.4\mu_B$ and $\approx 1.8\mu_B$, respectively. In addition, between 3 and 50 K temperatures, canting of Fe and Cr moments was also observed. Furthermore, two new peaks appeared in low-*T* data ($\leqslant$20 K) near $2\theta = 15.5^\circ$ {0 1 0}/{1 0 0} and near $2\theta = 27^\circ$ {0 1 2}/{1 0 2}, indicating the ordering of the Nd moments. The *ab*-plane pseudosymmetry in the two reflections indicates that the moments should lie in the **ab** plane. The thermal evolution of magnetic peak intensities (presented in Fig. S7 in the Supplemental Material [34]) shows that while the intensity of the {0 1 3} peak at 3 K is reduced by $\approx 35\%$ compared with its 20 K counterpart, the intensity of the {0 1 1} peak remains almost unchanged. Therefore, we also considered the moment at the Nd site in the refinement of the 20 and 3 K scattering data. However, we were unable to extract the Nd contribution properly due to the very low intensity at these peak positions from the 20 K data.

The Rietveld refined diffraction pattern [42] measured at a temperature of 20 and 3 K are illustrated in Fig. 5(a) and 5(b). When fitted with BVs of IR1, the calculated intensity of the 3 K diffraction pattern [Fig. 5(b)] agrees with the experimental data. The values obtained of total magnetic moments at 3 K temperature are $\mu_{\mathrm{Fe}} = 1.40\mu_B$ ($\mu_a = -0.336$, $\mu_b = -1.318$, $\mu_c = 0.289$), $\mu_{\mathrm{Cr}} = 1.835\mu_B$ ($\mu_a = -0.535$, $\mu_b = 1.739$, $\mu_c = -0.245$) and $\mu_{\mathrm{Nd}} = 2.13\mu_B$ ($\mu_a = -1.117$, $\mu_b = 1.615$, $\mu_c = 0.820$), respectively, where μ_a, μ_b, *and* μ_c represent components of the moment along a, b, and c axes, respectively. At 3 K, the obtained value of the Nd moment is much less than its free ion value of $3.27\mu_B$, as expected for Nd^{3+}, but it agrees with the value reported in other Nd-based DPs [19,43] and Nd_2O_3 [44] systems.

Overall, the neutron-diffraction results reveal that the main Fe-Cr network adopts ferrimagnetic order. The magnetic structure studied at 3 K [shown in Fig. 5(c)] manifests a ferrimagnetic alignment of the Fe and Cr sublattices, mainly along the **b** direction, while the Nd moments form a canted structure aligned in the **ab** plane. The refinement of low-*T* data using the same propagation vector indicates a change within the existing magnetic structure caused by the ordering of Nd moments. There are several reports on Nd-based DP systems in which similar kinds of magnetic phase evolution have been found. However, in addition to the existing magnetic structure corresponding to $K = (0\,0\,0)$, a second distinct magnetic structure with a different propagation vector has been reported at low temperatures (primarily below 15 K) [23,43].

E. Muon spin spectroscopy

Muon spin spectroscopy [45,46] is a highly sensitive magnetic probe to explore the role of internal magnetic field in magnetic ordering, information on spin dynamics, magnetic volume fraction [47], the superconducting vortex state [48,49], etc. Because of its sensitivity to extremely small fluctuations in fields, it is an ideal technique for carefully investigating the temperature dependence of small changes in magnetism. Hence, to clarify whether the observed low-temperature anomaly originates from the magnetic ordering of the Nd ion, we performed weak transverse field (wTF) and zero field (ZF) μSR measurements in the broad temperature range of 5 to 480 K.

1. Weak transverse field (wTF) measurement

In the paramagnetic phase of the sample, the muon spin precesses under the applied transverse field. However, in the long-range ordered phase, the internal field developed causes muons to precess at a frequency corresponding to the internal magnetic field rather than the weak external magnetic field. Taking advantage of this, the magnetic transition temperature and the evolution of the magnetic volume fraction were determined by wTF measurements ($B = 30$ Oe). The obtained time spectra were fitted using equation (3), which defines the time dependence of muon asymmetry (A) as the oscillating decay function given below:

$$A(t) = A_0\, e^{-\lambda_0 t}\, \cos(2\pi f t + \phi), \tag{3}$$

where A_0 corresponds to the initial muon asymmetries of the oscillating part, λ_0 is the relaxation rate, f is the frequency of oscillation, and ϕ is the phase constant. The wTF time spectra for Nd_2FeCrO_6 recorded at selected temperatures are illustrated in Fig. 6(a). In the paramagnetic phase (measured

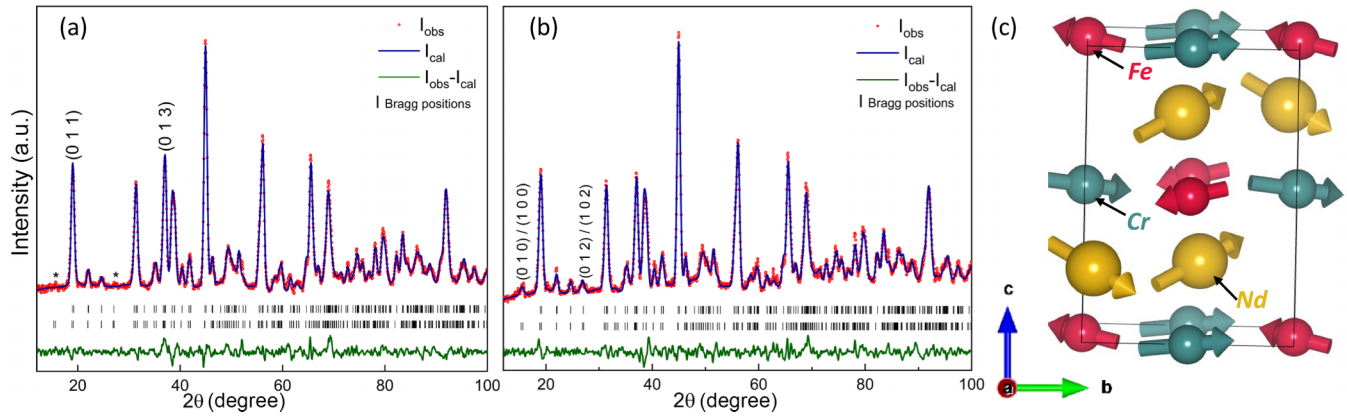

FIG. 5. Combined nuclear and magnetic refined neutron diffraction pattern of NFCO at (a) 20 K and (b) at 3 K with $P2_1/n$ space group. Red circle denotes the observed intensity I_{obs}, blue solid line represents calculated intensity I_{cal}, black vertical sticks are the allowed Bragg reflections and the bottom green line is the difference between observed and calculated intensity ($I_{obs} - I_{cal}$). (c) Schematic representation of the magnetic structure of NFCO at 3 K. Spheres with arrows in pink, cyan, and golden color represent moments on Fe, Cr, and Nd atoms, respectively.

at 480 K), muons oscillate at a frequency determined by the externally applied magnetic field. With a decrease in temperature, the loss of asymmetry increases, and oscillations disappear below the transition temperature. This infers that the internal magnetic field is substantially greater than the applied magnetic field. Since the amplitude of the oscillatory component A_0 corresponds to the paramagnetic fraction of the sample, the thermal dependence of A_0 captures the evolution of the magnetic phase in the system. Figure 6(b) summarizes the variation in A_0 and the magnetic volume fraction as a function of temperature. In the process of going from low to high temperatures, an abrupt change in A_0 (red circle curve) near 250 K reflects the transition from a static ordered state to a dynamic disordered state, concomitant with the magnetic data. However, complete asymmetry is achieved only above 460 K, which indicates that the magnetic contribution is present at high temperatures. The magnetic volume fraction was estimated using the formula $V_{mag}(T) = 1 - A_0(T)/A_0(T_{paramagnetic})$ and fitted with equation (4) [50],

$$V_{mag}(T) = V_{mag}(0)\,\frac{1}{2}\left[1 - \mathrm{erf}\left(\frac{T - T_N}{\sqrt{2}\Delta T}\right)\right], \qquad (4)$$

where erf is the error function, T_N is the transition temperature, $V_{mag}(0)$ is the magnetic volume fraction at 0 K, and ΔT is the transition width. The parameters obtained are $T_N \approx 257.87$ K and $V_{mag}(0) \approx 98.56\%$, indicating the presence of a fully magnetized state at low temperatures. A nonzero magnetic volume fraction above the transition temperature appears due to the Fe moments that survive at high temperatures, as indicated by neutron diffraction and DC magnetization data.

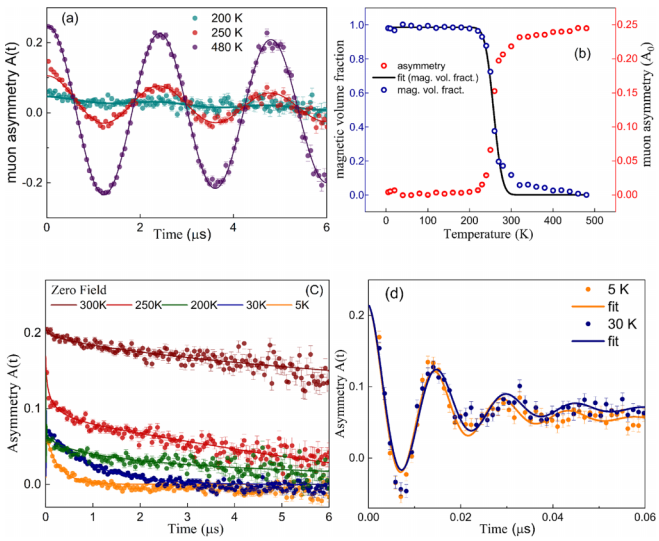

FIG. 6. (a) μSR asymmetry of NFCO recorded at $T = 480$, 250, and 200 K in the presence of a weak transverse magnetic field (wTF) of 30 Oe. Circles represent the experimental data points, and the solid lines are corresponding fits to the data using equation (3). (b) Temperature dependence of muon spin asymmetry A_0 (yellow open circles) and magnetic volume fraction (blue open circles). The black solid line is the fit to the magnetic volume fraction using equation (4). (c) Zero field (ZF) μSR time spectra of NFCO recorded at several selected temperatures. Colored circles represent the experimental data, and the corresponding fits using equation (5) are shown by the solid lines. (d) ZF μSR asymmetry plotted on a shorter timescale at 30 and 5 K.

2. *Zero-field (ZF) measurement*

The zero-field (ZF) μSR measurements provide a comprehensive insight into the magnetic ordering and spin dynamics in systems showing complex magnetic behavior. Figure 6(c) represents ZF-μSR spectra measured at selected temperatures between 5 and 440 K. Below the transition temperature T_N, a characteristic drop in the initial asymmetry was observed. In a longer timescale window, the relaxation describes the spin dynamics corresponding to the longitudinal components of the internal field parallel to the muon spin polarization; while on a shorter timescale ($t < 0.1$ μs), the appearance of fast damped oscillation indicates a static internal field distribution perpendicular to muon spin polarization. Therefore, the presence of a well-defined muon spin oscillation at low temperatures, as shown in Fig. 6(d), indicates a commensurate magnetically ordered state. The ZF time spectra were fitted

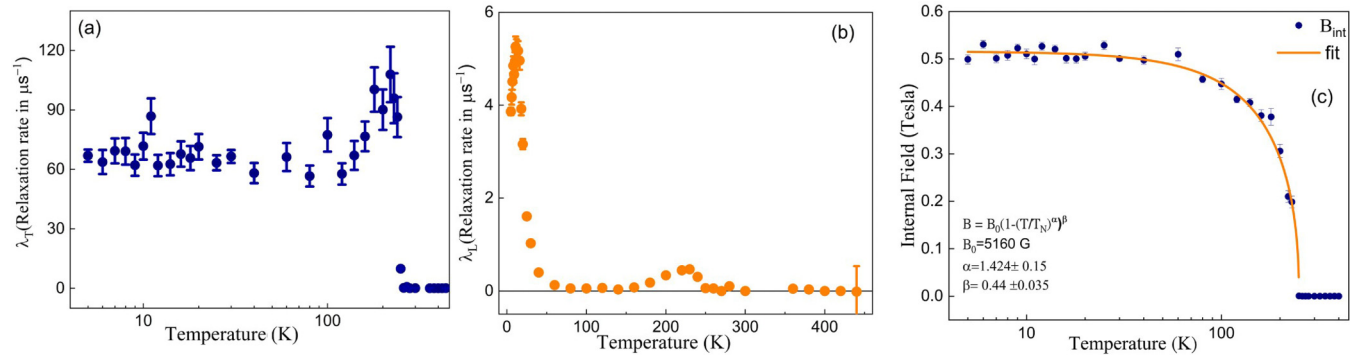

FIG. 7. (a) Temperature dependence of transverse muon spin-relaxation rate λ_T (temperature on a log scale) and (b) longitudinal relaxation rate λ_L. (c) Evolution of the order parameter (B_{int}) with temperature on a log scale. The solid yellow line corresponds to the fit using equation (6).

with a function defined by equation (5):

$$A(t) = \tfrac{2}{3}A_T\, e^{-\lambda_T t}\, \cos(2\pi f t + \phi) + \tfrac{1}{3}A_L e^{-\lambda_L t}, \qquad (5)$$

where the factor $2/3$ represents the magnetic field component perpendicular to the muon spin causing oscillations, the factor $1/3$ represents the longitudinal field component that does not cause oscillations, λ_T is the transverse relaxation rate, and λ_L is the longitudinal relaxation rate arising due to the dynamic magnetic fluctuation.

The temperature dependence of the internal field B_{int}, determined by the frequency of oscillation in muon asymmetry ($f_\mu = \gamma_\mu/2\pi\ B_{\text{int}}$), is shown in Fig. 7(c). A gradual increase in B_{int} is observed below 250 K, which saturates to a value of ≈ 0.5 T at low temperatures, representing a second-order magnetic phase transition. Furthermore, to gain more information about the system in its ordered state, the temperature dependence of B_{int} was fitted to equation (6) [51,52], which yields $T_N = 250$ K, $B_{\text{int}}(0) \approx 0.5$ T, $\alpha \approx 1.424$ and $\beta \approx 0.44$.

$$B_{\text{int}}(T) = B_{\text{int}}(0)\left[1 - \left(\frac{T}{T_N}\right)^{\alpha}\right]^{\beta}, \qquad (6)$$

where α corresponds to the low-temperature properties ($T \ll T_N$), governed by spin-wave excitation, and β describes the properties near the critical temperature. The factor β is close to the value predicted by the mean-field model ($\beta = 0.5$), while the exponent α follows Bloch's $T^{\frac{3}{2}}$ law of spin wave in a ferromagnet [15].

Since muon spin-relaxation rates capture the spin dynamics, it gives a fair understanding of the magnetic ordering, dynamics, and spin correlation in the system. The thermal dependence of relaxation rates λ_T and λ_L, illustrated in Figs. 7(a) and 7(b), shows some interesting features of the present system. The transverse relaxation rate λ_T, which encapsulates the distribution width and fluctuation of the internal field ($\Delta B = \lambda_T/\gamma_\mu$), has a high value of $\approx 65\ \mu s^{-1}$ at 5 K. This implies a broad magnetic field distribution at the muon sites. Moreover, a sharp increase in λ_T is observed at T_N, which decays and tends to saturate with decreasing temperature. Here, it must be noted that near 11 K a slight enhancement in the value is detected, which cannot be ignored.

The temperature dependence of the longitudinal spin-lattice relaxation rate λ_L is captured in Fig. 7(b), which arrests dynamic fluctuation. It has a temperature-dependent behavior similar to that of the DC magnetization trend. Near T_N, it shows the characteristic peak, and after that it decreases to zero with decreasing temperature indicating magnetization going towards the static limit. It is interesting to note that below 50 K, an upturn occurs in λ_L, forming a strong peak at around ≈ 11 K. This suggests a second phase transition in the system. At this temperature, the value of λ_L is almost five times the value observed at 250 K temperature, which decreases subsequently. These features in λ_L and in λ_T fall in the same temperature range in which the upturn in C_p/T vs T, the broad hump in C_p, and the negative magnetization in DC magnetization were observed.

F. Theoretical calculations

We first examined the spin polarized band structure of the experimentally observed ferrimagnetic states of Nd_2FeCrO_6 with $U_{\text{Fe}} = 3.75$ eV and $U_{\text{Cr}} = 2.75$ eV, as shown in Fig. 8(a). An insulating state with a direct band gap of ≈ 1.8 eV is clearly seen at the C_2 point in the down-spin channel. The bands near the Fermi level in this channel have a dominant contribution from Fe and Cr d orbitals. We emphasize here that inclusion of U is not necessary to drive the system insulating, and only imposing a magnetic ground state brings a band gap of ≈ 0.75 eV. Hence, one can conclude that the *true* electronic structure of Nd_2FeCrO_6 results from the combination of magnetism and electronic correlation. To experimentally estimate the value and nature of the band gap, we performed UV-Vis spectroscopy in the 500 to 800 nm wavelength range. The band gap is calculated using the equation $\alpha h\nu = A(h\nu - E_g)^n$, developed by Davis and Mott [53]. As shown in Fig. 8(b), fitting the plot of $(\alpha h\nu)^2$ vs $h\nu$ yields a direct band gap of 1.73 eV. This value is very close to the theoretically calculated value of the bang gap (E_g).

In the magnetic ground state, each of the Fe atoms has six Cr atoms as the first neighbor, and vice versa. This coupling is antiferromagnetic, and the magnetic moments on the Fe and Cr sites are $4.18\mu_B$ and $2.68\mu_B$, respectively, in this case. This is quite close to experimentally observed values. We find that this antiferromagnetic ground state is stabilized by ≈ 79 meV over the ferromagnetic state. Estimated $J_{\text{Fe-Cr}}$ with the procedure mentioned in Sec. II gives $J_{\text{Fe-Cr}} \approx$

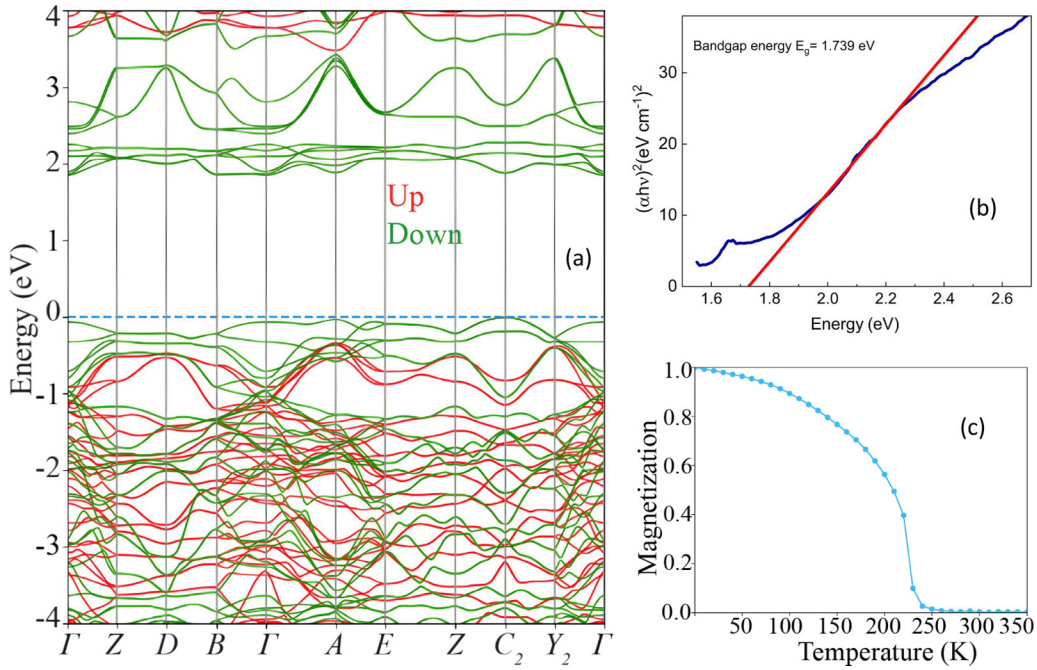

FIG. 8. (a) Spin-polarized band structure plot for the antiferromagnetic ground state of Nd_2FeCrO_6. A direct band gap of ≈ 1.8 eV is found in the down-spin channel which has contributions from both the Fe and Cr ions. The Fermi energy is set to zero. (b) Plot of $(\alpha h\nu)^2$ vs energy $h\nu$ for NFCO to determine the band gap using the Davis and Mott equation. (c) Plot of normalized magnetization as a function of temperature for Nd_2FeCrO_6 obtained with the antiferromagnetic first neighbor $J_{\text{Fe-Cr}} \sim -13$ meV.

-13 meV. The corresponding plot of normalized magnetization obtained from the MC simulation is shown in Fig. 8(c). Our calculations give $T_N \approx 230$ K, which is quite close to the experimentally observed value of 250 K.

IV. DISCUSSIONS AND CONCLUSION

The temperature dependence of DC magnetization points towards a ferrimagnetic behavior caused by the ordering of two TM atoms, as predicted theoretically. Interestingly, an anomalous second transition, as shown in Fig. 2(a), was also observed where the magnetization below 15 K becomes negative. This can be understood as some moments getting aligned in a direction opposite to the direction of initial magnetization. Such low-temperature behavior is not uncommon and has been observed in rare-earth-based systems. What fascinates the most is the source of the peculiarity because it strongly depends on the magnetic nature of the A site atom (which in this case is paramagnetic) and the surrounding environment created by other atoms. Our detailed investigation using macroscopic and microscopic techniques reveals some fascinating features around this temperature related to the ordering of Nd moments. Here, we discuss such features and the origin of the magnetic anomaly.

The local site symmetry and CEF anisotropy created by surrounding atoms may alter the electronic structure of rare-earth ions. The CEF removes the spin-orbit-coupled $(2J + 1)$-fold degeneracy of the ground state. In the case of the Kramer's ion, the ground state is a doublet and is considered to be a pseudospin-1/2 state having a finite moment. In this light, Nd^{3+} being a Kramer's ion with local C_1 site symmetry, CEF splits the total $J = 9/2$ into five ground-state doublets well separated in energy. The presence of such a pseudospin-1/2 moment in this system is indicated by the change in magnetic entropy ΔS_m. As discussed earlier, in zero field, this value comes out to be 5.76 J/(mol K), as expected for a $J_{\text{eff}} = 1/2$ system. Fitting the zero-field data below 20 K with a two-level Schottky function gives the lowest doublet splitting energy of ≈ 0.4 K, which is very small. Furthermore, as shown in Fig. 3(d), the thermal dependency of C_p/T vs T behavior shows an upturn below 14 K. These observations suggest coupling between pseudospin-1/2 moments of the Nd^{3+} ion. The broad hump in $C_p(T)$ at low temperature infers that the coupling is short ranged, which otherwise would show a λ-like anomaly. From these results, it appears that the CEF effect is contributing to determining the low-temperature ground state. However, inelastic neutron-scattering or temperature-dependent Raman-scattering measurements would be insightful for a complete understanding of CEF in this system and to comment on the energy scales of interaction. Such pseudospin-1/2 doublets of Nd^{3+} have also been reported in other Nd-based systems [54,55].

The neutron diffraction and muon spin spectroscopy results further corroborate our speculation of ordering of the Nd^{3+} pseudospin-1/2 moments. As discussed in Sec. III D, the thermal evolution of the neutron-diffraction peak profile shows the emergence of two new reflections on one hand and a reduction in the intensity of pre-existing {0 1 3} magnetic peaks on the other hand, happening simultaneously at low T ($\leqslant 20$ K). Meanwhile, a strong reduction in the values of magnetic moments in Fe and Cr atoms was observed in the same temperature range. This speaks of the substantial effect of the Nd ordering on other magnetic atoms present

in the system. Magnetic refinement of the peak considering the moment at the Nd site yielded $\mu_{\mathrm{Nd}} = 2.13\mu_B$, which is very close to the observed value of $2.37\mu_B$/Nd atom for a ground-state doublet [43,55,56]. Furthermore, the estimated magnetic structure contains Nd moments arranged opposite to the Fe-Cr sublattice magnetization, concomitant with the magnetic anomaly. The localized nature of probing combined with the greater sensitivity to small magnetic changes makes μSR an ideal microscopic lens to examine the Nd ordering in detail. wTF-μSR confirms a long-range ordering (LRO) below 250 K due to the presence of the TM-atom. If the $J_{\mathrm{eff}} = 1/2$ moments of Nd^{3+} undergo a second transition below 20 K, a further reduction of muon asymmetry is expected, which is not observed in this case. This may be due to the fact that the system had already achieved a fully ordered state above the Nd ordering temperature. In ZF-μSR, well-defined muon oscillations were observed at low temperatures, confirming the commensurate magnetic structure. The most striking features were observed in the relaxation rates. In addition to the first transition peak at 250 K, λ_L shows a second much stronger peak, kicking in below 50 K and maximizing at 11 K. Since λ_L is regarded as the reflection of dynamic fluctuation in the internal field at the muon site, a huge jump points to a very rapid arrangement of moments in this temperature range. This prominent feature in λ_L strongly supports the idea of 3D LRO of $J_{\mathrm{eff}} = 1/2$ moments of Nd^{3+} ions. Moreover, a slight enhancement in λ_T is observed at 11 K, which coincides with the peak position in λ_L and should not be ignored. This can be considered as a change in slope due to the second magnetic ordering. Similar behavior was also found for the pyrochlore system $Nd_2Ir_2O_7$ [57], in which the second peak was attributed to the ordering of Nd^{3+} moments. It is interesting to note that the internal field is almost constant, ignoring small fluctuations at low temperature, in contrast with the one observed in Ref. [57]. This could be due to the presence of high and rapid fluctuations, as indicated by the values of λ_L and λ_T.

For a given Nd moment of $2.13\mu_B$ and a distance (a) of separation ≈ 3.8 Å between two nearest neighboring Nd atoms, the magnetic dipolar interaction energy $E_{\mathrm{dip}} \approx \mu_0 g^2 \mu_B^2 / 4\pi a^3$ is proportional to $g^2/16$ (g is the Landé factor), which is very small. This implies a dominant superexchange interaction between $J_{\mathrm{eff}} = 1/2$ moments of Nd^{3+}. In conclusion, based on our investigation employing experimental techniques such as specific heat, neutron diffraction, and muon spin relaxation, we suggest that the bulk magnetization starts to fall as the LRO of $J_{\mathrm{eff}} = 1/2$ moments of Nd^{3+} starts to develop, in addition to the complex Nd-Fe/Cr interaction, below 50 K and compensates for the magnetization of the TM lattice. Eventually, below 15 K, when the moments are completely ordered, magnetization becomes negative. We believe that the present investigation offers a distinct origin behind the occurrence of negative magnetization in double-perovskite oxide systems from the unique presence of ordering in Nd, coupled with spin ordering in Nd and TM atoms. The combined investigation through μSR spectroscopy and neutron diffraction offers an atomistic insight into understanding the detailed origin of long-range ordering in a complex oxide system, which is an important step toward the development of oxide spintronics and quantum materials.

ACKNOWLEDGMENTS

The authors acknowledge the CeSAR (Centro Servizi d'Ateneo per la Ricerca) of the University of Cagliari (IT) for the magnetic characterization and the heat capacity measurements performed with the Quantum Design PPMS DynaCool. S.K. acknowledge the Council of Scientific and Industrial Research (CSIR), India, for the CSIR-JRF fellowship (File No. 09/1023(0043)/2020-EMR-I). This work was partially carried out using the facilities of UGC-DAE CSR, Indore. We acknowledge Mr. Sachin Kumar Dabaral, UGC-DAE CSR, Indore center, for his help during the XPS measurements. S.K.P. thanks NFSG grant from BITS-Pilani, Dubai campus, which supported this research. T.S. acknowledges financial support from the Swedish Research Council (VR Grant No. 2021-03675). G.M. and F.C. acknowledge funding from the European Union - Next-GenerationEU - National Recovery and Resilience Plan (NRRP)—MISSION 4 COMPONENT 2, INVESTIMENT N. 1.1, CALL PRIN 2022 PNRR D.D. 1409 14-09-2022—(HADES Half-metAllic Double-perovskites for next-genEration Spintronics) CUP N. P2022Y2BRK.

DATA AVAILABILITY

The data that support the findings of this article are not publicly available. The data are available from the authors upon reasonable request.

[1] A. A. Aczel, Q. Chen, J. P. Clancy, C. dela Cruz, D. Reig-i Plessis, G. J. MacDougall, C. J. Pollock, M. H. Upton, T. J. Williams, N. LaManna, J. P. Carlo, J. Beare, G. M. Luke, and H. D. Zhou, Spin-orbit coupling controlled ground states in the double perovskite iridates A_2BIrO_6 (A = Ba, Sr; B = Lu, Sc), Phys. Rev. Mater. **6**, 094409 (2022).

[2] O. Mustonen, S. Vasala, E. Sadrollahi, K. P. Schmidt, C. Baines, H. C. Walker, I. Terasaki, F. J. Litterst, E. Baggio-Saitovitch, and M. Karppinen, Spin-liquid-like state in a spin-1/2 square-lattice antiferromagnet perovskite induced by d^{10}–d^0 cation mixing, Nat. Commun. **9**, 1085 (2018).

[3] S. D. Bader and S. S. P. Parkin, Spintronics, Annu. Rev. Condens. Matter Phys. **1**, 71 (2010).

[4] A. Hirohata, K. Yamada, Y. Nakatani, I.-L. Prejbeanu, B. Diény, P. Pirro, and B. Hillebrands, Review on spintronics: Principles and device applications, J. Magn. Magn. Mater. **509**, 166711 (2020).

[5] S. H. Lee, H. C. Choi, and B.-J. Yang, Odd-parity spin-triplet superconductivity in centrosymmetric antiferromagnetic metals, Phys. Rev. Lett. **126**, 067001 (2021).

[6] M. P. Ghimire, L.-H. Wu, and X. Hu, Possible half-metallic antiferromagnetism in an iridium double-perovskite material, Phys. Rev. B **93**, 134421 (2016).

[7] K.-I. Kobayashi, T. Kimura, H. Sawada, K. Terakura, and Y. Tokura, Room-temperature magnetoresistance in an oxide material with an ordered double-perovskite structure, Nature (London) **395**, 677 (1998).

[8] B. Singh, D. Kumar, V. Kumar, M. Vogl, S. Wurmehl, S. Aswartham, B. Büchner, and P. Kumar, Fractional spin fluctuations and quantum liquid signature in Gd_2ZnIrO_6, Phys. Rev. B **104**, 134402 (2021).

[9] A. Harbi, Y. L. E. Godec, H. Moutaabbid, S. Benmokhtar, and M. Moutaabbid, Tailoring the Griffiths-like cluster formation in the insulator ferromagnet spin-glass $Gd_2Ni_xCo_{1-x}MnO_6$ double perovskite, Phys. Rev. B **104**, 054404 (2021).

[10] P. C. Rout and U. Schwingenschlögl, Strain-attenuated spin frustration in double perovskite Sr_2FeOsO_6, Phys. Rev. B **103**, 024426 (2021).

[11] H. Wang, S. Zhu, X. Ou, and H. Wu, Ferrimagnetism in the double perovskite Ca_2FeOsO_6: A density functional study, Phys. Rev. B **90**, 054406 (2014).

[12] M. Sikora, O. Mathon, P. Van der Linden, J. M. Michalik, J. M. De. Teresa, C. Kapusta, and S. Pascarelli, Field-induced magnetostructural phase transition in double perovskite Ca_2FeReO_6 studied via x-ray magnetic circular dichroism, Phys. Rev. B **79**, 220402(R) (2009).

[13] H. Mutch, O. Mustonen, H. C. Walker, P. J. Baker, G. B. G. Stenning, F. C. Coomer, and E. J. Cussen, Long-and short-range magnetism in the frustrated double perovskite Ba_2MnWO_6, Phys. Rev. Mater. **4**, 014408 (2020).

[14] G. J. Nilsen, C. M. Thompson, C. Marjerisson, D. I. Badrtdinov, A. A. Tsirlin, and J. E. Greedan, Magnetic order and multipoles in the $5d^2$ rhenium double perovskite Ba_2YReO_6, Phys. Rev. B **103**, 104430 (2021).

[15] S. Blundell, *Magnetism in Condensed Matter* (Oxford University Press, Oxford, 2001).

[16] X. Chen, J. Xu, Y. Xu, F. Luo, and Y. Du, Rare earth double perovskites: A fertile soil in the field of perovskite oxides, Inorg. Chem. Front. **6**, 2226 (2019).

[17] F.-Y. Li, Y.-D. Li, Y. Yu, A. Paramekanti, and G. Chen, Kitaev materials beyond iridates: Order by quantum disorder and Weyl magnons in rare-earth double perovskites, Phys. Rev. B **95**, 085132 (2017).

[18] D. T. Adroja, Shivani Sharma, C. Ritter, A. D. Hillier, Duc Le, C. V. Tomy, R. Singh, R. I. Smith, M. Koza, A. Sundaresan *et al.*, Muon spin rotation and neutron scattering investigations of the B-site ordered double perovskite Sr_2DyRuO_6, Phys. Rev. B **101**, 094413 (2020).

[19] A. A. Aczel, D. E. Bugaris, J. Yeon, C. de la Cruz, H.-C. zur Loye, and S. E. Nagler, Coupled Nd and B' spin ordering in the double perovskites $Nd_2NaB'O_6$ ($B' = $ Ru, Os), Phys. Rev. B **88**, 014413 (2013).

[20] T. Ferreira, S. Calder, D. S. Parker, M. H. Upton, A. S. Sefat, and H.-C. zur Loye, Relationship between A-site cation and magnetic structure in $3d$-$5d$-$4f$ double perovskite iridates Ln_2NiIrO_6 ($Ln = $ La, Pr, Nd), Phys. Rev. Mater. **5**, 064408 (2021).

[21] J. Sánchez-Benítez, M. J. Martínez-Lope, J. A. Alonso, and J. L. García-Muñoz, Magnetic and structural features of the $NdNi_{1-x}Mn_xO_3$ perovskite series investigated by neutron diffraction, J. Phys.: Condens. Matter **23**, 226001 (2011).

[22] S. Pal, S. Jana, S. Govinda, B. Pal, S. Mukherjee, S. Keshavarz, D. Thonig, Y. Kvashnin, M. Pereiro, R. Mathieu, P. Nordblad, J. W. Freeland, O. Eriksson, O. Karis, and D. D. Sarma, Peculiar magnetic states in the double perovskite Nd_2NiMnO_6, Phys. Rev. B **100**, 045122 (2019).

[23] C. Ritter, S. Sharma, and D. T. Adroja, Magnetic structures of the iridium-based double perovskites Pr_2NiIrO_6 and Nd_2NiIrO_6 reinvestigated using neutron diffraction, Phys. Rev. Mater. **6**, 084405 (2022).

[24] M. Sun, Y. Xuan, G. Liu, Y. Liu, F. Zhang, J. Ren, and M. Chen, Anomalous magnetic behaviors of double perovskite R_2CrFeO_6 (R = rare earth elements) predicted by first-principles calculations, J. Magn. Magn. Mater. **504**, 166670 (2020).

[25] J. Rodriguez-Carvajal, Fullprof: a program for Rietveld refinement and pattern matching analysis, in *Satellite Meeting on Powder Diffraction of the XV Congress of the IUCr, Toulouse, France* (Scientific Research Publishing Inc., 1990), Vol. 127.

[26] R. Delhez and E. J. Mittemeijer, Winplotr: A windows tool for powder diffraction pattern analysis, Mater. Sci. Forum **378**, 118 (2001).

[27] A. Suter and B. M. Wojek, Musrfit: A free platform-independent framework for μSR data analysis, Phys. Procedia **30**, 69 (2012).

[28] G. Kresse and D. Joubert, From ultrasoft pseudopotentials to the projector augmented-wave method, Phys. Rev. B **59**, 1758 (1999).

[29] P. E. Blöchl, Projector augmented-wave method, Phys. Rev. B **50**, 17953 (1994).

[30] G. Kresse and J. Furthmüller, Efficient iterative schemes for *ab initio* total-energy calculations using a plane-wave basis set, Phys. Rev. B **54**, 11169 (1996).

[31] John P. Perdew, K. Burke, and M. Ernzerhof, Generalized gradient approximation made simple, Phys. Rev. Lett. **77**, 3865 (1996).

[32] S. L. Dudarev, G. A. Botton, S. Y. Savrasov, C. J. Humphreys, and A. P. Sutton, Electron-energy-loss spectra and the structural stability of nickel oxide: An LSDA + U study, Phys. Rev. B **57**, 1505 (1998).

[33] M. T. Anderson, K. B. Greenwood, G. A. Taylor, and K. R. Poeppelmeier, B-cation arrangements in double perovskites, Prog. Solid State Chem. **22**, 197 (1993).

[34] See Supplemental Material at http://link.aps.org/supplemental/10.1103/c87f-xf83 for anomalous magnetism in the $3d$-$4f$ double perovskite oxide Nd_2FeCrO_6 with the Kramers ion Nd^{3+}.

[35] M. A. Islam, T. Sato, F. Ara, and M. A. Basith, Sol-gel based synthesis to explore structure, magnetic and optical properties of double perovskite Y_2FeCrO_6 nanoparticles, J. Alloys Compd. **944**, 169066 (2023).

[36] S. Sharma, D. T. Adroja, C. Ritter, D. Khalyavin, P. Manuel, G. B. G. Stenning, A. Sundaresan, A. D. Hillier, P. P. Deen, D. I. Khomskii, and S. Langridge, Magnetic ground state of the ordered double-perovskite Sr_2YbRuO_6: Two magnetic transitions, Phys. Rev. B **102**, 134412 (2020).

[37] W. Schnelle, J. Engelhardt, and E. Gmelin, Specific heat capacity of Apiezon N high vacuum grease and of Duran borosilicate glass, Cryogenics **39**, 271 (1999).

[38] Z. Jirák, J. Hejtmánek, K. Knížek, P. Novák, E. Šantavá, and H. Fujishiro, Magnetism of perovskite cobaltites with Kramers rare-earth ions, J. Appl. Phys. **115**, 17E118 (2014).

[39] A. Singh, S. Rajput, P. Balasubramanian, M. Anas, F. Damay, C. M. N. Kumar, G. Eguchi, A. Jain, S. M. Yusuf, T. Maitra, and V. K. Malik, Successive spin reorientations and rare earth ordering in $Nd_{0.5}Dy_{0.5}FeO_3$: Experimental

and *ab initio* investigations, Phys. Rev. B **102**, 144432 (2020).

[40] J. Rodríguez-Carvajal, BasIreps: A Program for Calculating Irreducible Representations of Little Groups and Basis Functions of Polar and Axial Vector Properties. Part of the FullProf Suite of Programs (Institut Laue-Langevin, 2010), http://www.ill.eu/sites/fullprof/.

[41] M. D. I. Bhuyan, R. Hossain, F. Ara, and M. A. Basith, A first-principles study on the phase stability and physical properties of a B-site ordered Nd_2CrFeO_6 double perovskite, Phys. Chem. Chem. Phys. **24**, 1569 (2022).

[42] H. M. Rietveld, A profile refinement method for nuclear and magnetic structures, J. Appl. Crystallogr. **2**, 65 (1969).

[43] H. Guo, C. Ritter, Y. Su, A. C. Komarek, and J. S. Gardner, Distinct magnetic ground states of R_2ZnIrO_6 (R = La, Nd) determined by neutron powder diffraction, Phys. Rev. B **103**, L060402 (2021).

[44] G. Sala, M. B. Stone, B. K. Rai, A. F. May, C. R. DelaCruz, H. SuriyaArachchige, G. Ehlers, V. R. Fanelli, V. O. Garlea, M. D. Lumsden, D. Mandrus, and A. D. Christianson, Physical properties of the trigonal binary compound Nd_2O_3, Phys. Rev. Mater. **2**, 114407 (2018).

[45] A. D. Hillier, S. J. Blundell, I. McKenzie, I. Umegaki, L. Shu, J. A. Wright, T. Prokscha, F. Bert, K. Shimomura, A. Berlie, H. Alberto, and I. Watanabe, Muon spin spectroscopy, Nat. Rev. Methods Primers **2**, 4 (2022).

[46] M. G. Flokstra, S. J. Ray, S. J. Lister, J. Aarts, H. Luetkens, T. Prokscha, A. Suter, E. Morenzoni, and S. L. Lee, Measurement of the spatial extent of inverse proximity in a Py/Nb/Py superconducting trilayer using low-energy muon-spin rotation, Phys. Rev. B **89**, 054510 (2014).

[47] S. J. Ray, A. S. Gibbs, S. J. Bending, P. J. Curran, E. Babaev, C. Baines, A. P. Mackenzie, and S. L. Lee, Muon-spin rotation measurements of the vortex state in Sr_2RuO_4: Type-1.5 superconductivity, vortex clustering, and a crossover from a triangular to a square vortex lattice, Phys. Rev. B **89**, 094504 (2014).

[48] D. O. G. Heron, S. J. Ray, S. J. Lister, C. M. Aegerter, H. Keller, P. H. Kes, G. I. Menon, and S. L. Lee, Muon-spin rotation measurements of an unusual vortex-glass phase in the layered superconductor $Bi_{2.15}Sr_{1.85}CaCu_2O_{8+\delta}$, Phys. Rev. Lett. **110**, 107004 (2013).

[49] R. Khasanov, T. Kondo, M. Bendele, Y. Hamaya, A. Kaminski, S. L. Lee, S. J. Ray, and T. Takeuchi, Suppression of the antinodal coherence of superconducting $(Bi, Pb)_2(Sr, La)_2CuO_{6+\delta}$ as revealed by muon spin rotation and angle-resolved photoemission, Phys. Rev. B **82**, 020511(R) (2010).

[50] X. Y. Zhu, H. Zhang, D. J. Gawryluk, Z. X. Zhen, B. C. Yu, S. L. Ju, W. Xie, D. M. Jiang, W. J. Cheng, Y. Xu, M. Shi, E. Pomjakushina, Q. F. Zhan, T. Shiroka, and T. Shang, Spin order and fluctuations in the $EuAl_4$ and $EuGa_4$ topological antiferromagnets: A μSR study, Phys. Rev. B **105**, 014423 (2022).

[51] P. D. De Réotier and A. Yaouanc, Muon spin rotation and relaxation in magnetic materials, J. Phys.: Condens. Matter **9**, 9113 (1997).

[52] R. Pelka, P. Konieczny, M. Fitta, M. Czapla, P. M. Zielinski, M. Bałanda, T. Wasiutyński, Y. Miyazaki, A. Inaba, D. Pinkowicz, B. Sieklucka, Magnetic systems at criticality: Different signatures of scaling, Acta Phys. Pol. A **124**, 977 (2013).

[53] J. I. Pankove, *Optical Processes in Semiconductors* (Courier Corporation, 1975).

[54] B. Singh, M. Vogl, S. Wurmehl, S. Aswartham, B. Büchner, and P. Kumar, Kramers doublets, phonons, crystal-field excitations, and their coupling in Nd_2ZnIrO_6, Phys. Rev. Res. **2**, 023162 (2020).

[55] M. Watahiki, K. Tomiyasu, K. Matsuhira, K. Iwasa, M. Yokoyama, S. Takagi, M. Wakeshima, and Y. Hinatsu, Crystalline electric field study in the pyrochlore $Nd_2Ir_2O_7$ with metal-insulator transition, J. Phys.: Conf. Ser. **320**, 012080 (2011).

[56] H. Guo, C. Ritter, and A. C. Komarek, Direct determination of the spin structure of $Nd_2Ir_2O_7$ by means of neutron diffraction, Phys. Rev. B **94**, 161102(R) (2016).

[57] H. Guo, K. Matsuhira, I. Kawasaki, M. Wakeshima, Y. Hinatsu, I. Watanabe, and Z.-A. Xu, Magnetic order in the pyrochlore iridate $Nd_2Ir_2O_7$ probed by muon spin relaxation, Phys. Rev. B **88**, 060411(R) (2013).

Correction: A missing statement has been added to the Acknowledgment section.